RSC Advances

PAPER

View Article Online
View Journal | View Issue

Cite this: *RSC Adv.*, 2019, **9**, 40607

Highly reactive energetic films by pre-stressing nano-aluminum particles†

Michael N. Bello,[a] Alan M. Williams,[a] Valery I. Levitas,[b] Nobumichi Tamura,[c] Daniel K. Unruh,[d] Juliusz Warzywoda[e] and Michelle L. Pantoya *[a]

Received 27th June 2019
Accepted 15th November 2019

DOI: 10.1039/c9ra04871e

rsc.li/rsc-advances

Energetic films were synthesized using stress altered nano-aluminum particles (nAl). The nAl powder was pre-stressed to examine how modified mechanical properties of the fuel particles influenced film reactivity. Pre-stressing conditions varied by quenching rate. Slow and rapid quenching rates induced elevated dilatational strain within the nAl particles that was measured using synchrotron X-ray diffraction (XRD). An analytical model for stress and strain in a nAl core–Al_2O_3 shell particle that includes creep in the shell and delamination at the core–shell boundary, was developed and used for interpretation of strain measurements. Results show rapid quenching induced 81% delamination at the particle core–shell interface also observed with Transmission Electron Microscopy (TEM). Slower quenching elevated dilatational strain without delamination. All films were prepared at approximately a 75 : 25 Al : poly(vinylidene fluoride) PVDF weight ratio and were 1 mm thick. A drop weight impact test was performed to assess ignition sensitivity and combustion. Stress altered nAl exhibited greater energy release rates and more complete combustion than untreated nAl, but reaction dynamics and kinetics proceeded in two different ways depending on the nAl quenching rate during pre-stressing.

Introduction

Metal particles such as aluminum (Al) are used in films for a variety of applications including protective coatings against friction and wear,[1] light scattering optical coatings,[2] electronic device performance,[3] catalysis[4] as well as energy generating applications.[5,6] The chemical energy stored inherently within an Al particle (85 GJ m^{-3}) makes it an attractive candidate for energy conversion applications but there are still challenges for Al combustion. Specifically, harnessing stored chemical energy within an Al particle effectively requires engineering that will: (1) increase the rate of energy release upon ignition and (2) increase complete consumption of the Al fuel particle upon combustion.

One promising approach to address both challenges is based on the metallurgical process of pre-stressing that is accomplished by annealing and quenching Al powder. Pre-stressing deliberately induces strain within the core–shell particle structure and has been shown to enhance the reactivity of micrometer diameter Al particles (μAl).[7–9] Recent research has shown quenching rate has a significant effect on strain evolution in μAl particles.[8] Specifically, rapid quenching (*i.e.*, super-quenching) leads to delamination at the core–shell interface that results in stress relaxation and a reduction in the measured dilatational strain. With an Al_2O_3 shell unsupported by the Al core, super-quenching enables more exposure of the Al core for rapid oxidation once ignited especially under impact conditions. All previous studies involving super-quenched Al powder were performed with μAl, but the mechanics of delamination that result from super-quenching should extend to nano-aluminum (nAl) particles also.

Additive manufacturing (AM) has advanced significantly in recent years, extending its capabilities into the processing of energetic materials that include nAl particles.[6] Blade casting is an AM approach for preparing energetic films and is based on extrusion of a slurry, similar to fused deposition modeling (FDM) (another AM synthesis approach). The slurry combines fuel and oxidizer powders with a binder and solvent and the blade casting process involves drawing a blade over the slurry to create a film of controlled thickness. Blade casting has been employed in the additive manufacturing of films for batteries

[a]*Department of Mechanical Engineering, Texas Tech University, Lubbock, TX 79409, USA. E-mail: michelle.pantoya@ttu.edu; Tel: +1-806-834-3733*

[b]*Departments of Aerospace Engineering and Mechanical Engineering, Iowa State University and Ames Laboratory, Division of Materials Science and Engineering, Ames, IA 50011, USA*

[c]*Advanced Light Source, Lawrence Berkeley National Laboratory, Berkeley, CA 94720, USA*

[d]*Department of Chemistry, Texas Tech University, Lubbock, TX 79409, USA*

[e]*Materials Characterization Center, Whitacre College of Engineering, Texas Tech University, Lubbock, TX 79409, USA*

† Electronic supplementary information (ESI) available: Representative photograph of all films examined in this study. Powder X-ray diffraction spectrum and Rietveld refinement compositional analysis for all pre- and post-combustion films. Description of analytical model development for nanoparticles. See DOI: 10.1039/c9ra04871e

and capacitors[10,11] and for rapid prototype manufacture of laminated ceramic components.[12]

Blade casting for thermal battery applications was used to synthesize thin energetic films made from powders of magnesium (Mg) and manganese dioxide (MnO_2) that were combined with several solvent–binder systems.[13] Meeks *et al.*[13] demonstrated that the solvent–binder system had an important role in the homogeneity of the cured film and influenced film combustion. A solvent–binder system composed of *N*-methylpyrrolidone (NMP) and polyvinylidene fluoride (PVDF) resulted in improved energy release rates attributed to a more homogenous powder distribution in the film.

Merging newly developed stress altered Al powder with binders commonly used in additive manufacturing is an important advancement in the development of energetic films and their processing. The objectives of this study were to examine the effects of stress altered nAl particles on films cast with PVDF binder. Specifically, three effects were characterized: (1) strain associated with nAl particles pre-stressed using two quenching rates; (2) transmission electron microscopy analysis of the stress altered core–shell particles; and, (3) impact ignition and combustion of stress altered nAl + PVDF films. The stress altered nAl particles were characterized using synchrotron X-ray diffraction (XRD) to quantify dilatational strain. An analytical model was also developed to quantify delamination at the core–shell interface of nAl particles required to understand the strain measurements as a function of quenching rate. The films were prepared by mixing nAl powder with PVDF binder and co-solvent to form slurries that were blade cast into ~1 mm thick films. The reactivity of the films was examined upon ignition using a drop weight impact tester. The goal was to improve the reactive properties of nAl by using pre-stressing to alter the mechanical, structural and chemical properties of the particles and facilitate their application as films in the science of materials.

Experimental

Materials

Spherical Al particles with an 80 nm average particle diameter and 4 nm amorphous aluminum oxide shell (Novacentrix, Austin, TX) were used in this study. The solvents included acetone and dimethylformamide (DMF); both were reagent grade and supplied from Macron Fine Chemicals (Center Valley, PA) and EMD Millipore (Burlington, MA), respectively. The binder was poly(vinylidene fluoride) (PVDF) (molecular weight = 534 000) supplied from Sigma Aldrich (St. Louis, MO).

Aluminum powder pre-stressing

All pre-stressed aluminum (PS nAl) powders were annealed and quenched in a controlled thermal environment using a Q800 DMA (Dynamic Mechanical Analyzer) from TA Instruments (New Castle, DE). The annealing and quenching procedure is detailed in Hill *et al.*[7] but summarized here for completeness. Annealing was accomplished in an air environment with a heating rate of 0.166 K s^{-1} to 573 K then held for 15 minutes. The quenching rate for PS nAl was on average 1.47 K s^{-1}. Quenching with liquid nitrogen was programmed at an exponential rate from the annealing temperature to ambient according to eqn (1) with $A = 0.0078\ s^{-1}$, ambient temperature, $T_a = 298$ K, anneal temperature, $T_0 = 573$ K, with time t in seconds. Eqn (1) models lumped capacitance cooling and the heating and cooling transients are illustrated elsewhere.[7]

$$T = T_a + (T_0 - T_a)\exp(-At) \quad (1)$$

The super-quenched aluminum (SQ nAl) powder was annealed and quenched in a custom-built chamber designed to survive high thermal gradients associated with rapid quenching. This process is detailed elsewhere[8] but summarized here for completeness. Annealing was accomplished in a Vulcan multi-stage programmable furnace in an air environment at a heating rate of 0.166 K s^{-1} up to 573 K. The sealed powder chamber is quenched by immersion in a liquid solution comprised of water, salt, dish soap, and commercial surfactants. The solution produces a quenching rate on average of 11.14 K s^{-1}, an order of magnitude faster than PS nAl.

Synchrotron XRD measurements of strain

The dilatational strain for all nAl powders was measured using Synchrotron X-ray Diffraction (XRD) at the Advanced Light Source facility, Lawrence Berkeley National Laboratory on beamline 12.3.2 using a micron focused synchrotron X-ray beam. Measurements from this beamline that quantify dilatational strain in μAl powder have been reported previously.[14–17] In contrast to previous measurements on μAl powder, data on the nAl particles were taken with a 10× 2μ 12 keV monochromatic beam because the size from the white beam focus (around 1 μ) was not sufficiently small to resolve the nAl particles. For the nAl particles, data were taken in 'powder diffraction pattern' mode and dilatational strain was derived from the shifts in 2θ values of the powder rings with respect to their 'unstrained' positions. Powder patterns were taken with the detector at an angle of 50° and distance of 18 cm from the powder sample. Fig. S1A and B† show example powder patterns obtained from the stress altered nAl particles. Data were processed using XMAS software and details of the experimental setup and synchrotron XRD capabilities are described elsewhere.[18]

Powder TEM characterization

All nAl powders were imaged using a Hitachi H-9500 transmission electron microscope (TEM) at 300 kV. Powders were suspended in ethanol, sonicated, and deposited on a Lacey Formvar stabilized with carbon support film deposited on 400 mesh Cu grids (Ted Pella, product # 01885).

Film preparation

The films include stress altered nAl powders: PS nAl or SQ nAl and were compared with untreated nAl powder (UN nAl). Each nAl powder was mixed with a binder–solvent system that includes PVDF, acetone, and DMF. The volume of the DMF–acetone co-solvent was constant and the initial masses of PVDF

and nAl were constant at a 50 weight percent Al : PVDF ratio. It is noted that during film processing some of the PVDF evaporates with the slurry such that the final film composition is approximately 75 : 25 wt% Al : PVDF (see below). Also, the global Al + PVDF reaction is shown in eqn (2) indicating condensed phase products that include carbon (soot) and AlF_3. It is noted that flame temperatures for this reaction have recently been measured to be ~1500 K.[19]

$$2Al + 3C_2H_2F_2 \rightarrow 2AlF_3 + 6C + 3H_2 \quad (2)$$

For film preparation, 500 mg of PVDF was dissolved in a co-solvent of acetone and DMF. For every gram of the total material, 7 mL (2 mL DMF and 5 mL acetone) of co-solvent was used to make a solution suitable for mixing in a DAC 150.1 FVZ-K SpeedMixer™ (FlackTek Inc.). The solution was mixed for 45 seconds at 2000 rpm in the SpeedMixer™ to ensure PVDF was completely dissolved. Then, 0.5 g of nAl (UN, PS, and SQ) was added to the solution prior to loading in the SpeedMixer™ for continued processing at 2000 rpm for an additional 5 minutes.

Once mixing was completed, the suspension was blade cast onto a 50 μm thick stainless-steel foil substrate using a draw-down blade film applicator. A thin slit gap in the film applicator ensures uniform deposition thickness because the thickness of the film is equal to the gap height of the blade. This blade extrusion apparatus has been detailed previously and used to successfully prepare energetic thin films.[20] The films were air dried in a fume hood, then transferred to a vacuum chamber for 24 hours to evaporate the solvent then recovered from the substrate and cut using a razor blade to appropriate sample size for further characterization.

A photograph showing each film (Fig. S1C†) is included in ESI.† The PXRD analysis of the films are shown in Fig. S2.1 in ESI† and indicate that the composition of each film ranges from 72–74 wt% Al with 20–24 wt% PVDF and the remaining composition includes trace amounts of aluminum nitride (AlN) indicating some reaction between the Al particles and DMF from the solvent during film preparation, and $Ca(CO_3)$ attributed to the PXRD sample holder. This result implies that some PVDF dissolved in the acetone and DMF solution evaporated during film drying because the precursor included a 50 : 50 wt% Al : PVDF concentration. The amorphous content in all films is attributed to poorly crystalline PVDF with peaks that match when comparing pure PVDF to the film in Fig. S2.2 of ESI.†

Reactivity characterization

A schematic of the impact tester is shown in Fig. 1. Impact is from a carriage that rides on ball bearing pillow blocks along guide rails with an attached steel striker to impact the intermediate weight on a pressure cell. The full picture of the apparatus is shown in Fig. 1a. The pressure cell is shown in Fig. 1b with both a photograph and schematic better illustrating its internal operation. The pressure cell houses a 50 mg film and this sample mass was held constant throughout all experiments. The pressure cell enables more than just analysis of ignition but also overall reaction with two built in sensors for measuring transient pressure and light intensity. The maximum energy that can be delivered by the striker carriage is 42 J and is controlled by the drop height (maximum of 0.91 m) and carriage weight (maximum of 6.172 kg), both are adjustable. In these experiments impact ignition energy of 2.5 J mg^{-1} were delivered to all films. For all samples the drop height was 0.91 m and carriage weight was 6.172 kg.

Instrumentation in the pressure cell to characterize the combustion event includes a PCB Piezotronics pressure sensor (PCB 101A06) (Fig. 1). The pressure sensor records a pressure-time history within the cell that provides insight into ignition and extent of reaction (Fig. 1). The measurement range is 3450 kPa with a 1.45 mV kPa^{-1} sensitivity and low frequency response of 400 kHz. Raw data from each experiment is filtered using a low-pass filter cutoff at 4 kHz and data were collected at 100 kHz.

Fig. 1 includes a representative pressure history plot. Measurements from the pressure sensor include maximum peak pressure, rise time to peak pressure, pressurization rate, and area under the pressure time curve. Maximum peak pressure is the highest point of the pressure curve and rise time to peak pressure is the time from inflection to 80% of the maximum pressure which is defined as the end of reaction for the purpose of consistency. Pressurization rate is the pressure gradient during pressure rise, and pressure-area is the integral area under the pressure as a function of time curve using trapezoidal numerical integration, beginning at the inflection and ending at 80% of the maximum pressure.

PXRD for species identification

Powder X-ray diffraction (PXRD) analysis was performed on the pre- and post-combustion materials to identify composition of the crystalline species. A Rigaku MiniFlex II powder diffractometer utilizing Cu Kα radiation (1.5418 Å), was operated in continuous θ–2θ mode from 5–90° 2θ with Bragg–Brentano geometry. The step size was 0.02° with a collection time ranging from 0.1 to 0.5° min^{-1} depending upon the sample. The MDI Jade V9.1.1 software provided both qualitative and quantitative data analysis used to determine the presence and concentration of AlF_3 within the samples. Diffractograms of the samples with peak matches are shown in ESI† along with the Rietveld refinement difference profiles.

Results

Fig. 2 shows the dilatational strain distribution, average strain, and standard deviation from PS nAl and SQ nAl that result from the annealing and quenching treatments. The untreated (UN) nAl powder has a very small residual strain (*i.e.*, 0.6% (ref. 21)) and was not included in this analysis due to limited time allotted for synchrotron XRD analysis. Annealing and quenching increases particle strain, and quenching rate has a measurable effect on strain. The distribution presented in Fig. 2 is obtained by performing several measurements. The powder is spread on a flat surface and raster scanned, taking diffraction

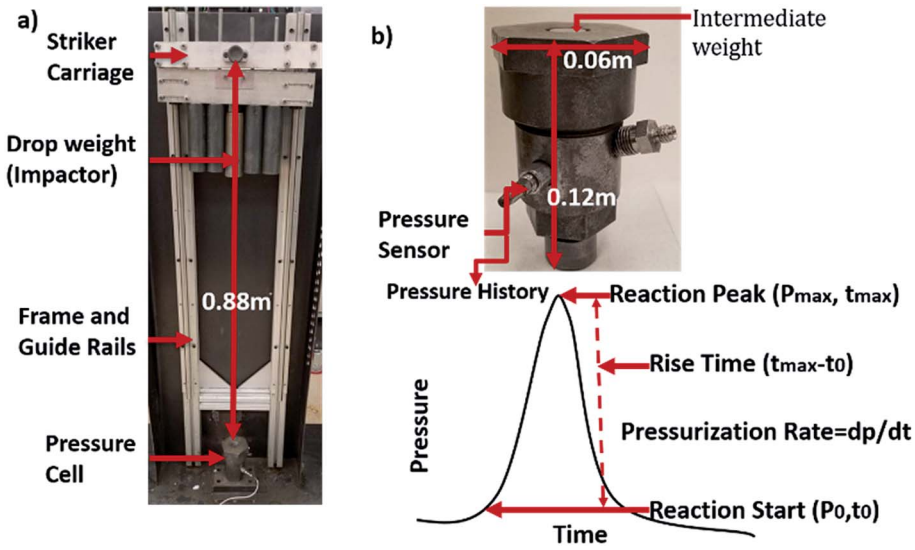

Fig. 1 Photographs of the drop weight apparatus. (a) Full scale view with labeled striker carriage, drop weight impactor, frame with guide rails, and pressure cell. The distance from the carriage to pressure cell is 0.88 m. (b) Enlargement of pressure cell with labeled sensor. Representative data from the pressure sensor is also illustrated.

patterns at each step, and over a thousand patterns were collected. The average strain shown in Fig. 2 is approximately an order of magnitude greater than similar measurements for micron-scale Al particles (see Hill *et al.*[8]) and consistent with the theoretical analysis shown below. Theoretically, a higher quenching rate should result in higher strain,[22] but Fig. 2 indicates that the higher quenching rate reduced strain. Hill *et al.*[8] observed a similar trend in strain with quenching rate for μAl powder. They modeled the development of strain and theorized that strain relaxation in the SQ μAl powder was attributed to delamination at the core–shell particle interface. Modeling delamination is extended to nAl powder measurements below.

Three distinctive curves representative of single combustion events corresponding to films with UN nAl + PVDF, PS nAl + PVDF, and SQ nAl + PVDF are shown in Fig. 3, and data comparing pressure responses are shown in Table 1. Pressure histories were examined for peak pressure, rise time, pressurization rate (representative of reaction rate), and the area under the pressure curve (representative of the extent and duration of combustion). Post combustion product species are also shown in Table 1, with detailed spectra provided in Fig. S2.3 in ESI.† It is noted that Table 1 shows the inclusion of potassium (K) containing species. While potassium was not present in the pre-combustion films, as evidenced in the PXRD data that is also included in ESI,† potassium containing species were detected in all post-combustion residue *via* PXRD. Trace elements from the alloy material comprising the pressure cell within the drop weight impact chamber may have participated in combustion including potassium, K.

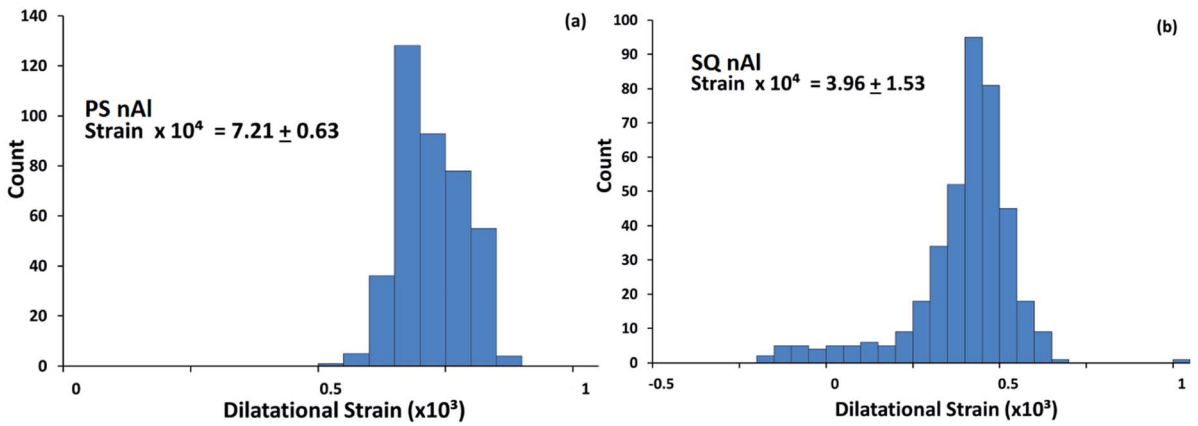

Fig. 2 Distribution of dilatational strain for (a) PS nAl and (b) SQ nAl particles, with average dilatational strain and standard deviation indicated in each figure.

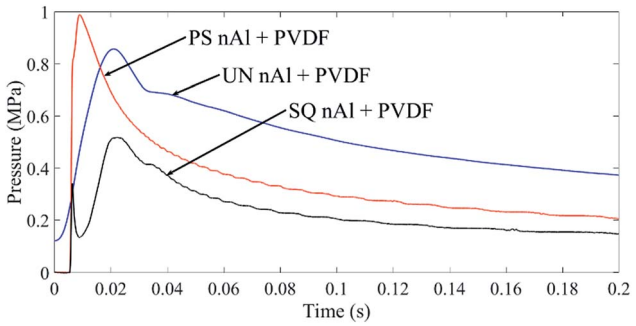

Fig. 3 Representative pressurization curves for untreated (UN), pre-stressed (PS), and super-quenched (SQ) nAl + PVDF films during impact ignition and combustion.

There are three interesting observations from analysis of the data in Table 1 (and Fig. 3). First, in comparison to UN nAl + PVDF, the PS nAl + PVDF film demonstrates a 25% higher peak pressure and order of magnitude higher pressure curve area. In contrast, the SQ nAl + PVDF film shows the lowest peak pressure and pressure curve area. Higher peak pressure correlates to greater gas generation during reaction. Overall, the PS nAl + PVDF film exhibits greatest gas generation. Because the starting mass and composition for all films are the same, the conclusion from Table 1 is that energy conversion during PS nAl + PVDF reaction leads to greater gas generation. Table 1 also indicates higher concentrations of K_2AlF_5 in the PS nAl + PVDF film product residue. The formation of K_2AlF_5 has been observed at low temperatures (*i.e.*, 873 K) with hydrofluoric acid (HF).[23,24] DeLisio *et al.*[25] observed for PVDF reacting with Al particles, oxidation takes place due to the production of HF gas when PVDF decomposes. The higher K_2AlF_5 concentrations from combustion of the PS nAl + PVDF film implies that the reaction kinetics associated with PS nAl + PVDF are favored in the gas phase involving HF to transform Al into K_2AlF_5. It is also noted that a lower temperature mechanism favors K_2AlF_5 formation over AlF_3.[23,24] Wang *et al.*[19] show the flame temperature of an Al + PVDF film is ~1500 K and the distribution of temperature within the reacting film can range widely suggesting regions that could thermally favor K_2AlF_5 over AlF_3 formation. Future work will elaborate more thoroughly on the evolution of temperature in reactions involving stress altered powders, but these results suggest that the greater gas generation over a longer duration associated with combustion of PS nAl + PVDF films also disperses thermal energy enabling lower temperature kinetics to dominate evidenced by the formation of K_2AlF_5.

Second, the SQ nAl + PVDF and PS nAl + PVDF films exhibit a significantly faster pressurization (Table 1). The pressurization rate is indicative of the reaction rate upon ignition and thus stress altering particles has the effect of increasing the rate of reaction. The SQ nAl + PVDF exhibits a two-stage pressure rise: an initial spike followed by a slower rise suggesting a two-stage ignition and reaction behavior. In this case, the extended rise time to peak pressure may allow HF gas generated in the confined cell to react with Al and favor production of condensed phase AlF_3 as shown by Padhye *et al.*[26] For the second-stage in the SQ nAl + PVDF reaction there is similarity in the pressure history for the UN nAl + PVDF reaction with a plateau in pressure following the peak. The shoulder could be related to gas generation behavior which is more rate limited in these two films and may be produced in stages.

Third, there is significantly more condensed phase fluorinated species (K_2AlF_3 and AlF_3) in the stress altered films post-combustion residue (Table 1). Higher AlF_3 concentration in SQ nAl + PVDF film is consistent with the observation that there is less gas generation (lower peak pressure, longer rise time to peak pressure, and pressure curve area) because higher temperature and condensed phase kinetics favor AlF_3 formation while longer reacting PS nAl + PVDF films may produce a faster reacting environment favoring formation of K_2AlF_3. This observation is also consistent with the higher concentration of unreacted Al in the post combustion residue of UN nAl + PVDF films.

Modeling

The modeling objective is to control internal stresses in the core and shell that are described by the temperature T_0 at which shell is stress-free. Annealing at 573 K leads to creep in the shell that relaxes internal stresses and changes T_0 to 573 K. Quenching with an infinite cooling rate excludes stress relaxation and generates maximum tensile mean stress in the Al core and compressive hoop stress in a shell, assuming that there is no delamination at the core–shell boundary. However, if the normal stress at the core–shell interface σ_0 reaches or exceeds the critical stress for delamination, σ_{cd} (eqn (3)), then partial or complete delamination of the shell takes place.

Table 1 Peak pressure, pressure curve area, pressurization rate, rise time to peak pressure, and AlF_3, K_2AlF_5, and Al wt% from PXRD analysis of post combustion residue for UN nAl + PVDF, PS nAl + PVDF, and SQ nAl + PVDF films. Values highlighted are to emphasize interesting comparison differences. Note two-stage pressurization rate for SQ nAl + PVDF film with two reported rise times

Film	Peak pressure (MPa)	Pressure curve area (kPa s)	Pressurization rate (MPa s^{-1})	Rise time (ms)	wt% AlF_3	wt% Al	wt% K_2AlF_5
UN nAl + PVDF	0.86 ± 0.1	2.85 ± 0.2	46.10 ± 16.2	19.20	62	14	15
PS nAl + PVDF	**1.1 ± 0.2**	**11.52 ± 0.9**	**892.84 ± 12.9**	**3.44**	62	4	**34**
SQ nAl + PVDF	0.52 ± 0.1	0.42 ± 0.8	**890.88 ± 10.5/36.07 ± 2.55**	**0.9/13.13**	**83**	**5**	10

$$\sigma_0 \geq \sigma_{cd}, \quad (3)$$

A finite cooling rate results in partial stress relaxation during cooling due to creep in the shell. Stress relaxation at room temperature occurs slowly[16] and will be neglected.

Fig. 2 shows dilatational strain in the core was larger for PS nAl particles (*i.e.*, for slower quenching) than for SQ nAl particles (*i.e.*, for rapid quenching), like the results for μAl particles in ref. 8. We can use the same interpretation of the results in Fig. 2: for SQ nAl creep does not have time to occur but delamination takes place as soon as the criterion in eqn (3) is met. For PS nAl, creep occurs during quenching and the delamination criterion in eqn (3) is not reached.

Stresses and strain in the core–shell structure for the general case

Due to the thin Al_2O_3 shell, $\delta = 4$ nm, creep strain is assumed to be distributed uniformly in the shell. In contrast to modeling μAl particles, the effect of surface energy and stresses will be included for nAl particles. Due to plastic incompressibility eqn (4) holds, where ε_c^r and ε_c^h are the radial and hoop creep strain.

$$\varepsilon_c^r = -2\varepsilon_c^h \quad (4)$$

For nAl, the ratio of the particle radius (*i.e.*, $R + \delta$) to the nAl core radius (*i.e.*, R) is $m = (R + \delta)/R = 1 + 1/M$, with $M = R/\delta$ and cannot be considered very close to unity, as for μAl particles.[16,17] Since creep strain is not isotropic, a simple generalization for the equations for thermoelastic μAl particles presented in ref. 27 and 28 is impossible. That is why expressions for stresses and strains in the core and shell have been derived in ESI.† Here, eqn (S.15) and (S.16)† are generalized in a simplified way to include delamination of the shell from the core. Thus, the mean stress (negative pressure) in the Al core, σ_0, and hoop stress in the shell at the boundary with the core, σ_h can be obtained in eqn (5)–(7).

$$\sigma_0 = \left(\frac{12G_2K_1K_2\left((m^3-1)\left(\varepsilon_2{}^T - \varepsilon_1{}^T\right) + 3\varepsilon_c^h m^3 \ln m\right)}{H} - \frac{2\Gamma_2 m^2 K_1(4G_2+3K_2)}{RH}\right)(1-d) - \frac{2K_1(4G_2+3m^3K_2)((1-d)\Gamma_1 + \Gamma_{Al}d)}{RH}; \quad (5)$$

$$\varepsilon_0 = \frac{\sigma_0}{K_1}; \quad \varepsilon_1{}^T = \alpha_1(T-T_0); \quad \varepsilon_2{}^T = \alpha_2(T-T_0). \quad (7)$$

Here $H = 3m^3K_1K_2 + 4G_2(K_1 + (m^3-1)K_2)$, subscripts 1 and 2 designate Al and Al_2O_3, respectively, G and K are the shear and bulk moduli, Γ_1, Γ_2, and Γ_{Al} are the surface energies at the core–shell, shell–gas, and core–gas interfaces, ε_0 is the elastic dilatational strain in a Al core, which is measured in the synchrotron XRD experiments and reported in Fig. 2, α is the linear thermal expansion coefficient, and d is the damage parameter (degree of delamination). Parameter d characterizes (in a simplified averaged way) the degree of delamination of the shell from the core: *i.e.*, for $d = 0$ there is no delamination and for $d = 1$ there is complete delamination at the shell–core interface.

The degree of delamination is the ratio of the delaminated area to the total area of the particle at the core–shell interface averaged over all particles. Some particles may not delaminate at the core–shell interface, others may completely delaminate, and d represents an effective damage parameter that reproduces an average dilatational strain in the ensemble of particles. Eqn (5) and (6) generalize equations that were published in ref. 27 and 28 for the case with creep and damage. The case of eqn (5) and (6) with creep but for μAl particles (*i.e.*, with significant simplification for small $m - 1$) and without damage was presented in ref. 18; but, damage for μAl particles was included in ref. 8. The differences between μAl particles in ref. 8 and nAl particles in eqn (5) and (6) are:

(a) Eqn (5) and (6) include terms with surface tension: Γ_1, Γ_2, and Γ_{Al}. Damage is included as a linear interpolation in a way that after complete delamination ($d = 1$) the effect of the alumina-air surface tension Γ_2 disappears and the effect of Al–Al_2O_3 surface tension Γ_1 is substituted with the Al-air surface tension, Γ_{Al}.

(b) Instead of using simplified equilibrium equations, a strict analytical solution is used in eqn (5) and (6).

(c) Eqn (5) and (6) include a more complex expression for all terms due to the nanoscale dimensionality of the Al core, *i.e.*, non-small $m - 1$. In particular, the effects of the creep and thermal strains are not additive but have some weighting factors.

Equations for Al core–Al_2O_3 shell

All material and particle parameters are collected in Table 2.

When material parameters and R from Table 2 are inserted in eqn (5) and (6), they specify to eqn (8) and (9).

$$\sigma_h = \left(-\frac{6(m^3+2)\left(\varepsilon_2{}^T - \varepsilon_1{}^T\right)G_2K_1K_2}{H} - \frac{18\varepsilon_c^h G_2K_2(4G_2K_2(m^3-1-3m^3 \ln m) + K_1(4G_2+3K_2m^3+2(2G_2-3K_2)m^3 \ln m))}{(4G_2+3K_2)H}\right)(1-d) - \frac{2\Gamma_2 m^2(-2G_2K_1+3(2G_2+K_1)K_2)}{RH}(1-d) - \frac{4(m^3+2)G_2K_2((1-d)\Gamma_1+\Gamma_{Al}d)}{RH}; \quad (6)$$

Table 2 Material parameters for Al (subscript 1) and Al_2O_3 (subscript 2) at room temperature[18]

K_1 (GPa)	K_2 (GPa)	G_2 (GPa)	α_1 (10^5 K^{-1})	α_2 (10^5 K^{-1})	$\Gamma_1 = \Gamma_2 = \Gamma_{Al}$ (GPa nm)	R (nm)	δ (nm)
76	252	163	2.33	0.54	1.05	36	4

$$\sigma_0 = \big(-669.06(m^3-1)(T-T_0) + 1.1238394\times10^8\varepsilon_c^h m^3 \ln m - 6242.1m^2\big)\frac{1-d}{H} - \frac{2890.5+3351.6m^3}{H};\quad H = -114752 + 221760m^3 \tag{8}$$

$$\sigma_h = \big(334.530(m^2+2)(T-T_0) - 2.93\big(-0.205549 + 0.397226m^3 - m^3 \ln m\big)\times10^8\varepsilon_c^h - 16282.9m^2\big)\frac{1-d}{H} - \frac{4792.2(m^3+2)}{H}. \tag{9}$$

Further, after substituting δ from Table 2, *i.e.*, for $m = 10/9$, solutions shown in eqn (10)–(12) are obtained.

$$\sigma_0 = (-0.00131(T-T_0) + 85.737\varepsilon_c^h - 0.04068)(1-d) - 0.03953; \tag{10}$$

$$\sigma_h = (0.00595(T-T_0) - 301.469\varepsilon_c^h - 0.10611)(1-d) - 0.08529; \tag{11}$$

$$\varepsilon_0 = (-0.0000172(T-T_0) + 1.128\varepsilon_c^h - 0.00053)(1-d) - 0.00052. \tag{12}$$

Stress and strain after annealing followed by cooling: no damage

For $d = 0$, eqn (10)–(12) simplify to eqn (13)–(15).

$$\sigma_0 = -0.00131(T-T_0) + 85.737\varepsilon_c^h - 0.080; \tag{13}$$

$$\sigma_h = 0.00595(T-T_0) - 301.469\varepsilon_c^h - 0.191; \tag{14}$$

$$\varepsilon_0 = -0.0000172(T-T_0) + 1.128\varepsilon_c^h - 0.00105. \tag{15}$$

Let us discuss pre-stressing and stress relaxation based on eqn (8)–(12). For UN nAl particles, $\varepsilon_c^h = 0$, $d = 0$, and presumably $T = T_0 = T_r$, where T_r is room temperature. For this case, $\sigma_0 = -0.080$ GPa, $\sigma_h = -0.191$ GPa, and $\varepsilon_0 = -0.00105$, *i.e.*, both core and shell are under compression due to surface tension, and compressive strain in the core is quite large.

Since we neglected creep at room temperature, stress in the shell cannot relax. During annealing the increase in temperature ($T > T_0$) adds compressive (negative) mean stress σ_0 in the core and tensile (positive) hoop stress σ_h in the shell. Long annealing leads to relaxation of the hoop stresses due to creep, but in contrast to μAl particles,[27,28] stress in the nAl core cannot completely relax. Indeed, if we determine creep strain from the condition of no hoop stress in the shell at the boundary with the core ($\sigma_h = 0$) then eqn (16) expresses the creep strain in the shell where T_a is the annealing temperature.

$$\varepsilon_c^h = -0.00063 + 0.0000197(T_a - T_0) \tag{16}$$

Substituting eqn (16) in eqn (10) and (12) simplifies the core stress and strain into the following eqn (17) and (18), respectively.

$$\sigma_0^{rel} = -0.135 + 0.00038(T_a - T_0); \tag{17}$$

$$\varepsilon_0^{rel} = -0.00177 + 5.0\times10^{-6}(T_a - T_0). \tag{18}$$

From eqn (17) and (18), stress and strain in the Al core for fully relaxed shell depends on the difference between the annealing temperature and the temperature at which the shell is stress-free (coinciding with room temperature in this case). In these experiments, $T_0 = T_r = 298$ K, $T_a = 573$ K and the stress and strain in the core are given by eqn (19).

$$\sigma_0^{rel} = -0.030 \text{ GPa};\ \varepsilon_0^{rel} = -0.00040 \tag{19}$$

The results in eqn (19) show residual compressive stress and strain in the core at annealing temperature are much smaller than in the unrelaxed state at room temperature.

Now we can rewrite eqn (13)–(15) for new reference temperature $T_a = 573$ K at which there is no creep strain in the shell ($\sigma_h = 0$) and stress and strain in the core are determined by eqn (19). These new equations are shown in eqn (20)–(22) and indeed, for $\varepsilon_c^h = 0$ and $T = T_a$ we obtain $\sigma_h = 0$ and eqn (19).

$$\sigma_0 = -0.00131(T - T_a) + 85.737\varepsilon_c^h - 0.030; \tag{20}$$

$$\sigma_h = 0.00595(T - T_a) - 301.469\varepsilon_c^h; \tag{21}$$

$$\varepsilon_0 = -0.0000172(T - T_a) + 1.128\varepsilon_c^h - 0.00040. \tag{22}$$

For rapid quenching to room temperature $T = T_r$ and neglecting creep and damage, the results from eqn (20)–(22) are shown in eqn (23) for the maximum possible residual stress and strain.

$$\sigma_0(T_r) = 0.330 \text{ GPa};\ \sigma_h(T_r) = -1.636 \text{ GPa};\ \varepsilon_0(T_r) = 0.00435. \tag{23}$$

The value of the dilatational strain in eqn (23) is 0.00435 and significantly larger than the measured one 0.000396 (Fig. 2) consequently significant delamination of the shell should occur. The dilatational strain in eqn (23) is also much larger than the calculated dilatational strain of 0.0000113 for μAl particles ($M = 600$) after the same quenching shown in ref. 8.

At the same time the compressive hoop stress in the shell for μAl particles was also larger, −2.58 GPa, which is a desirable alteration that increases the strength of the shell and should delay ignition.

A lower value of measured dilatational strain for SQ nAl compared with calculations for undamaged particles means that the damage criterion in eqn (3) is met. The upper bound for theoretical stress for delamination $\sigma_{cd} = 0.330$ GPa that follows from eqn (23) is much higher than the value of 0.009 GPa obtained in ref. 8 for μAl particles. This is an expected scaling effect, similar to the large difference between theoretical strength for defect-free crystals and engineering strength for usual defective crystals. Indeed, the probability to find interfacial defects at the core–shell boundary is much smaller for nano-particles than for micron-particles, and many nano-particles may have a defect-free boundary.

Stresses and strains after annealing followed by cooling with delamination

Generalization of eqn (20)–(23) for the case with delamination during quenching without creep is shown in eqn (24)–(26).

$$\sigma_0 = (-0.00131(T - T_a) + 85.737\varepsilon_c^h + 0.00953)(1 - d) - 0.03953; \quad (24)$$

$$\sigma_h = (0.00595(T - T_a) - 301.469\varepsilon_c^h + 0.08529)(1 - d) - 0.08529; \quad (25)$$

$$\varepsilon_0 = (-0.0000172(T - T_a) + 1.128\varepsilon_c^h + 0.00012)(1 - d) - 0.00052, \quad (26)$$

The last term in eqn (24) and (25) is the contribution due to surface tension at the surface of nAl particles in eqn (10)–(12), which does not change with damage and remains for $d = 1$. The second limiting condition is that for $d = 0$, eqn (24)–(26) reduce to eqn (20)–(22). If eqn (26) for ε_0 at $\varepsilon_c^h = 0$ and $T = T_r$ is equal to the experimental value for SQ nAl particles, 0.000396, the result is $d = 0.81$. This value is larger than 0.52 obtained in ref. 8 for μAl particles. For this d and from eqn (24) and (25), $\sigma_0 = 0.030$ GPa and $\sigma_h = -0.380$ GPa.

For PS nAl, damage is neglected, and stresses partially relax by creep. Creep strain is determined by equating eqn (22) for ε_0 at $T = T_r$ to the experimental value for PS nAl particles, 0.000721; thus $\varepsilon_c^h = -0.00320$. For this case from eqn (20)–(22), $\sigma_0 = 0.055$ GPa and $\sigma_h = -0.671$ GPa.

Table 3 summarizes the particle stress and strain results from the analytical modeling. There are three interesting conclusions from examining the data in Table 3. First, annealing and quenching nAl powder flips the stress within the core from a state of tension to a state of compression. Second, in the ideal case of annealing and rapidly quenching with no delamination at the core and shell interface, the stress in the core and shell can increase by an order of magnitude. Third, using the measured values of strain for the case of SQ and PS nAl, the increase in stresses both in the core and shell nearly doubled, indicating that the PS nAl particles have the highest stresses as well as measured strain.

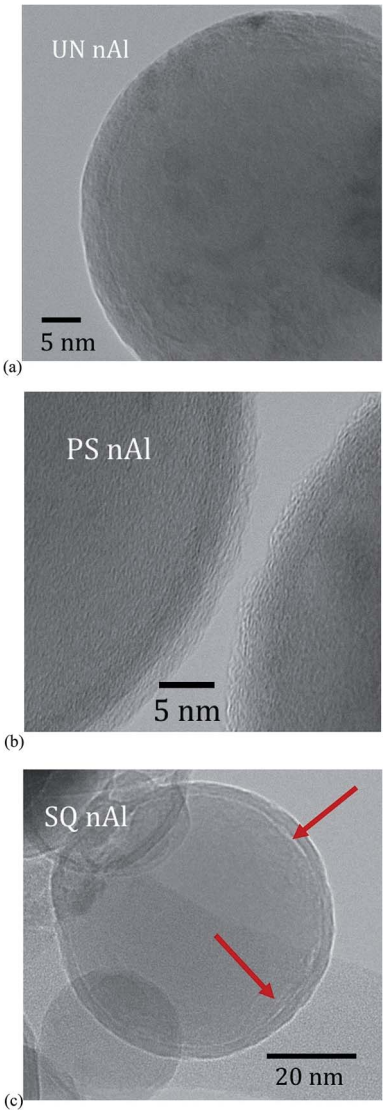

Fig. 4 TEM images of (a) UN nAl, (b) PS nAl, and (c) SQ nAl particles. Red arrows indicate regions of delamination.

Visualization of delamination using TEM

To identify delamination between the core and shell, nAl particles were analyzed using TEM. Fig. 4 shows images of UN nAl, PS nAl, and SQ nAl particles. Unlike the UN nAl and PS nAl particles (Fig. 4a and b), there is an indication of discontinuities at the core–shell boundary that may be attributed to delamination (Fig. 4c). Fig. 4 suggests confirmation of delamination predicted from the analytical modeling and the reduced strain measurements for SQ nAl particles compared to PS nAl particles.

Effect of particle size

Our experimental results (Fig. 2) show dilatation strain in nAl particles is almost an order of magnitude larger than for μAl in ref. 8 and can be explained from the model. While eqn (5)–(7) are relatively complex, in their simplified version for μAl (see eqn (5) in ref. 8), dilatational strain in a particle is proportional

Table 3 Summary of stress and strain results for a nAl particle. Note the * indicates measured strain values using synchrotron XRD

Description	Stress in particle core σ_0 GPa	Stress in shell at the boundary between core and shell σ_h GPa	Dilatational elastic strain ε_0
Untreated nAl (UN nAl)	−0.080	−0.191	-1.05×10^{-3}
Rapid quenching with no creep no delamination	0.330	−1.636	4.35×10^{-3}
Rapid quenching with delamination (SQ nAl)	0.030	−0.380	$*3.96 \times 10^{-4}$
Slow quenching with no delamination (PS nAl)	0.055	−0.671	$*7.21 \times 10^{-4}$

to d/R. Since oxide thickness d is the same for nano- and micron-scale particles, dilatational strain is in inverse proportion to R. Thus, without creep and delamination, dilatation in nanoparticles should be 500 times larger than for μAl. However, surface tension produces quite large (−0.0004) compressive strain, partially compensating this effect: the dilatational strain in eqn (23) is 0.00435 for nAl and 0.0000113 for μAl particles (M = 600) after the same quenching in ref. 8. The threshold for delamination for nAl is $\sigma_{cd} = 0.330$ GPa and much higher than 0.009 GPa obtained in ref. 8 for μAl powder, due to expected scale effect for strength. However, degree of delamination is larger for SQ nAl, which leads to significant relaxation of stresses and dilatation in comparison with SQ μAl particles. Creep strain in a shell of PS nAl is more than three times larger than for PS μAl, again leading to extra relaxation. A combination of all these competing factors quantitatively explains almost an order of magnitude larger dilatation strain in nAl compared with μAl.

Discussion

There are two different goals of pre-stressing nAl particles. The first is to produce and keep stresses as high as possible so that during heating in a reaction, tensile stresses in the shell will be smaller and fracture will be delayed to higher temperature or applied loading. Thus, stress relaxation during quenching should be minimized and can be achieved by sufficiently fast cooling.

An alternative goal is to produce partial or complete delamination of the shell from the core. A shell unsupported by the core will facilitate shell fracture and exposure of the oxidizer to the majority of core Al surface. For PS nAl particles, creep in the shell during quenching avoids shell–core delamination. For SQ nAl particles, creep in the shell does not have time to occur but delamination occurs at 81% of the core–shell interface, leading to lower internal stresses than for PS nAl particles. Fig. 4 provides a microscopic perspective of the core–shell interface and reveals regions of possible delamination.

Note that delamination at the core–shell boundary is a much more stochastic process, driven by the presence of the interfacial defects more than creep in an amorphous shell. The stochastic nature of delamination is evidenced in Fig. 2 that shows higher standard deviation of the dilatational strain for SQ nAl particles, for which some particles even have compressive strain. In contrast, for PS nAl particles, the distribution of dilatational strain is narrower and without particles with $\varepsilon_0 < 5 \times 10^{-4}$. Table 3 summarizes the modeled stresses and strains within nAl particles for four different cases. All stress altered particles transition from tensile to compressive stress within the core regardless of quenching. Also, PS nAl particles contain the highest stress for the measured dilatational strain nearly double from the SQ nAl particles.

Both quenching treatments affect film reactivity in comparison with UN nAl particles (see Table 1) indicating different reaction dynamics and kinetics occur with stress altered particles. Fig. 3 and Table 1 reveal that stress altered films produce faster reactions but PS nAl + PVDF films produce more gas generation during reaction as evident from higher peak pressure. The PXRD analysis in Table 1 is consistent with the pressure measurements because more condensed phase AlF_3 is formed from in the longer reaction time (longer rise time to peak pressure) associated with SQ nAl + PVDF but for PS nAl + PVDF films more gaseous fluorinated species are formed that favor K_2AlF_3 formation over condensed phase AlF_3. The different pressure responses and product species for PS nAl + PVDF and SQ nAl + PVDF films suggest the mechanisms for reaction and reaction kinetics associated with PS and SQ nAl are different.

Fig. 5 schematically depicts the differences in shell structure associated with UN nAl, PS nAl, and SQ nAl particles. Core–shell delamination in SQ nAl particles make the shell weaker without the core supporting its structure. A shell that is ~81% delaminated from the particle core will be more impact ignition sensitive. During impact, the level of shell failure in each sample is a function of the stress in the particles as well as the level of shell delamination. The UN nAl demonstrates the least shell failure represented by the fewest exposure sites in the shell (Fig. 5) and most unreacted Al in post combustion residue (Table 1). The PS nAl may incur significant spallation of the shell as stresses relax violently during impact (Fig. 5). Gaps in the SQ nAl shell during impact correspond to delaminated (white) regions before impact (Fig. 5). The SQ nAl demonstrates fracture and removal of delaminated shell that is unsupported. Levitas *et al.*[9] also suggest that damage in the form of nanovoids, inclusions, or decohesion at the core–shell interface are possible in addition to generation and relaxation of internal stresses as a result of quenching. Damage may result in aluminum diffusing through the shell and reacting with PVDF, producing additional internal stress and

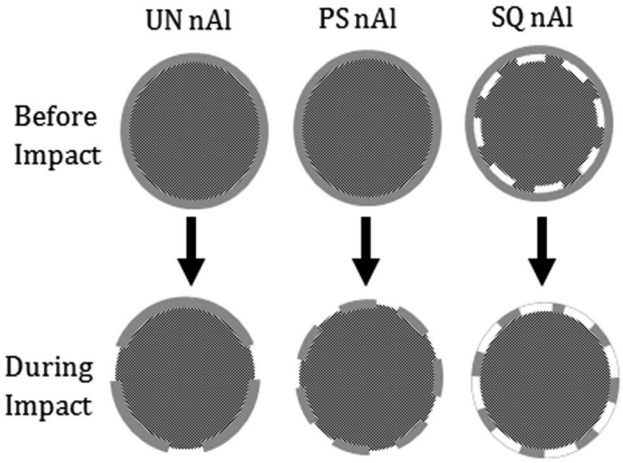

Fig. 5 Schematic representation of proposed differences in shell structures associated with UN, PS, and SQ nAl particles. The dark grey represents the crystalline aluminum core, and the light grey represents the amorphous alumina shell.

damage. Weakening the shell will cause fast reactions as seen by the high first stage pressurization rate for SQ nAl + PVDF and higher product concentration of condensed phase AlF_3. Interestingly, the initial fast energy release is followed by continued reaction at a slower rate ($\sim$36.07 MPa s^{-1}) indicating that SQ nAl + PVDF reactions proceed in two stages.

The PS nAl particles that do not experience delamination exhibit faster reaction times for the same impact energy as the SQ nAl + PVDF film. This theory is consistent with the PXRD results that show PS nAl + PVDF produces about as much AlF_3 as UN nAl + PVDF but higher concentrations of K_2AlF_5 favored in faster gas phase reactions involving HF, a primary decomposition product of PVDF.[19,25] The elevated strain energy inherent in PS nAl particles may also contribute towards more complete combustion, thus the low concentration of unreacted Al in the PS nAl + PVDF film (Table 1).

Conclusions

Films were prepared using strain altered nano-aluminum (nAl) powder and PVDF. The strain altered particles were prepared by annealing to 573 K then quenching at two different cooling rates: slow (1 K s^{-1}) and fast (11 K s^{-1}). Synchrotron XRD measurements revealed strain was lower for faster quenched nAl. While faster quenching should lock in higher strain, an analytical model for stress and strain in the nAl core–Al_2O_3 shell particle that includes creep in the shell and delamination at the core–shell boundary was developed and used for interpretation of dilatational strain measurements. Modeling results indicate 81% delamination between the particle core and shell was attributed to the reduced strain in the faster quenched powder. Transmission electron microscopy (TEM) of the nAl particles confirms delamination of rapidly quenched nAl particles. The slower quenched powder did not experience delamination, yet exhibited elevated strain.

The two different stress altered powders exhibited different reaction mechanisms as well as different reaction kinetics. The slower quenched (pre-stressed) nAl powder without delamination but with elevated strain exhibited more complete combustion compared to untreated nAl powder. More complete combustion was concluded from lower Al concentration in the product residue, greater gas generation, and shorter duration of reaction shown by higher peak pressure and shorter rise time to peak pressure. The pre-stressed nAl films also favor the formation of aluminum fluoride species formed from HF gas production during PVDF decomposition. In contrast, rapid quenching (super-quenched nAl) induces delamination at the core–shell interface that results in a two-stage ignition behavior: rapid reaction followed by a slower release of energy that was evidenced by higher initial pressurization rate and longer rise time to peak pressure that favors the formation of condensed phase AlF_3. The results presented here show that stress-altering aluminum particles has advantages for their impact induced reactivity but reaction dynamics and kinetics of the nAl particles are a strong function of pre-stressing treatment parameters, particularly quenching rate.

Conflicts of interest

There are no conflicts to declare.

Acknowledgements

The authors are grateful for support from Office of Naval Research under ONR contract N00014-16-1-2079 and N00014-19-1-2082 and our program managers, Dr Chad Stoltz and Mr Matthew Beyard. This work uses beamline 12.3.2, a resource at the Advanced Light Source, supported by the Director, Office 439 of Science, Office of Basic Energy Sciences, Materials Science Division, of the U.S. 440 Department of Energy under Contract No. DE-AC02-05CH11231 at LBNL.

References

1 J. T. Scheper, K. W. Mesthrige, J. W. Proscia, G.-Y. Liu and C. H. Winter, Atmospheric pressure chemical vapor deposition of titanium aluminum nitride films, *Chem. Mater.*, 1999, **11**, 3490–3496.
2 F. Cheng, P.-H. Su, J. Choi, S. Gwo, X. Li and C.-K. Shih, Epitaxial Growth of Atomically Smooth Aluminum on Silicon and Its Intrinsic Optical Properties, *ACS Nano*, 2016, **10**(11), 9852–9860.
3 H. M. Lee, H. B. Lee, D. S. Jung, J.-Y. Yun, S. H. Ko and S. B. Park, Solution processed aluminum paper for flexible electronics, *Langmuir*, 2012, **28**(36), 13127–13135.
4 W. Jiang, Z. Qiu, W. Yao, Y. Zhu and W. Cui, TiO_2/$Al(H_2PO_4)_3$ Composite Film as Separation-free and Washing-resistance Photocatalyst, *Appl. Catal., B*, 2017, **204**, 43–48.
5 K. J. Smith, Y. Cheng, E. S. Arinze, N. E. Kim, A. E. Bragg and S. M. Thon, Dynamics of Energy Transfer in Large Plasmonic Aluminum Nanoparticles, *ACS Photonics*, 2018, **5**(3), 805–813.

6 X. Li, P. Guerieri, W. Zhou, C. Huang and M. R. Zachariah, Direct deposit laminate nanocomposites with enhanced propellent properties, *ACS Appl. Mater. Interfaces*, 2015, **7**, 9103–9109.

7 K. J. Hill, J. Warzywoda, M. L. Pantoya and V. I. Levitas, Dropping the hammer: Examining impact ignition and combustion using pre-stressed aluminum powder, *J. Appl. Phys.*, 2017, **122**, 125102.

8 K. J. Hill, N. Tamura, V. I. Levitas and M. L. Pantoya, Impact ignition and combustion of micron-scale aluminum particles pre-stressed with different quenching rates, *J. Appl. Phys.*, 2018, **124**, 115903.

9 V. I. Levitas, J. McCollum and M. Pantoya, Pre-stressing micron-scale aluminum core-shell particles to improve reactivity, *Sci. Rep.*, 2015, **5**, 1–6.

10 E. Vidal, J. M. Rojo, M. C. García-Alegre, D. Guinea, E. Soto and J. M. Amarilla, Effect of composition, sonication and pressure on the rate capability of 5 V-$LiNi_{0.5}Mn_{1.5}O_4$ composite cathodes, *Electrochim. Acta*, 2013, **108**, 175–181.

11 G. N. Howatt, R. G. Breckenridge and J. M. Brownlow, Fabrication of thin ceramic sheets for capacitors, *J. Am. Ceram. Soc.*, 1947, **30**, 237–242.

12 X. Cui, S. Ouyang, Z. Yu, C. Wang and Y. Huang, A study on green tapes for LOM with water-based tape casting processing, *Mater. Lett.*, 2003, **57**, 1300–1304.

13 K. Meeks, M. L. Pantoya and C. Apblett, Deposition and characterization of energetic thin films, *Combust. Flame*, 2014, **161**, 1117–1124.

14 J. McCollum, M. L. Pantoya and N. Tamura, Improving aluminum particle reactivity by annealing and quenching treatments: Synchrotron X-ray diffraction analysis of strain, *Acta Mater.*, 2016, **103**, 495–501.

15 J. McCollum, D. K. Smith, K. J. Hill, M. L. Pantoya, J. Warzywoda and N. Tamura, A slice of an aluminum particle: Examining grains, strain and reactivity, *Combust. Flame*, 2016, **173**, 229–234.

16 V. I. Levitas, J. McCollum, M. L. Pantoya and N. Tamura, Stress relaxation in pre-stressed aluminum core–shell particles: X-ray diffraction study, modeling, and improved reactivity, *Combust. Flame*, 2016, **170**, 30–36.

17 V. I. Levitas, J. McCollum, M. L. Pantoya and N. Tamura, Internal stresses in pre-stressed micron-scale aluminum core–shell particles and their improved reactivity, *J. Appl. Phys.*, 2015, **118**, 094305.

18 M. Kunz, N. Tamura, K. Chen, A. A. MacDowell, R. S. Celestre, M. M. Church and E. Ustundag, A dedicated superbend X-ray microdiffraction beamline for materials, geo-, and environmental sciences at the advanced light source, *Rev. Sci. Instrum.*, 2009, **80**, 035108.

19 H. Wang, M. Rehwoldt, D. J. Kline, T. Wu, P. Wang and M. R. Zachariah, Comparison study of the ignition and combustion characteristics of directly-written Al/PVDF, Al/Viton, and Al/THV composites, *Combust. Flame*, 2019, **201**, 181–186.

20 B. Clark, J. McCollum, M. L. Pantoya, R. J. Heaps and M. A. Daniels, Development of flexible, free-standing, thin films for additive manufacturing and localized energy generation, *AIP Adv.*, 2015, **5**, 087128.

21 R. J. Jacob, K. J. Hill, Y. Yang, M. L. Pantoya and M. R. Zachariah, Pre-stressing aluminum nanoparticles as a strategy to enhance reactivity of nanothermite composites, *Combust. Flame*, 2019, **205**, 33–40.

22 J. F. Throop, J. H. Underwood and G. S. Legar, *Residual Stress and Stress Relaxation*, Plenum Press, 1971.

23 S. D. Kirik, Y. N. Zaitseva, D. Y. Leshok, A. S. Samoilo, P. S. Dubinin, I. S. Yakimov, D. A. Simakov and A. O. Gusev, NaF–KF–AlF_3 System: Phase Transition in $K_2NaAl_3F_{12}$ Ternary Fluoride, *Inorg. Chem.*, 2015, **54**, 5960–5969.

24 C. Rong, W. Genhua and Z. Qiyun, Phase diagram of the system KF–AlF_3, *J. Am. Ceram. Soc.*, 2000, **83**, 3196–3198.

25 J. B. DeLisio, X. Hu, T. Wu, G. C. Egan, G. Young and M. R. Zachariah, Probing the Reaction Mechanism of Aluminum/Poly(vinylidene fluoride) Composites, *J. Phys. Chem. B*, 2016, **120**(24), 5534–5542.

26 R. Padhye, A. J. A. Aquino, D. Tunega and M. L. Pantoya, Fluorination of an Alumina Surface: Modeling Aluminum–Fluorine Reaction Mechanisms, *ACS Appl. Mater. Interfaces*, 2017, **9**, 24290–24297.

27 V. I. Levitas, B. W. Asay, S. F. Son and M. Pantoya, Mechanochemical mechanism for fast reaction of metastable intermolecular composites based on dispersion of liquid metal, *J. Appl. Phys.*, 2007, **101**, 083524.

28 V. I. Levitas, Mechanochemical mechanism for reaction of aluminum nano- and micrometre-scale particles, *Philos. Trans. R. Soc., A*, 2013, **371**, 20120215.